Simulating infrared spectra and hydrogen bonding in cellulose Iβ at elevated temperatures

Vishal Agarwal,[1,a)] George W. Huber,[1,b)] W. Curtis Conner, Jr.,[1,c)] and Scott M. Auerbach[1,2,d)]
[1]*Department of Chemical Engineering, University of Massachusetts, Amherst, Massachusetts 01003, USA*
[2]*Department of Chemistry, University of Massachusetts, Amherst, Massachusetts 01003, USA*

(Received 10 May 2011; accepted 14 September 2011; published online 6 October 2011)

We have modeled the transformation of cellulose Iβ to a high temperature (550 K) structure, which is considered to be the first step in cellulose pyrolysis. We have performed molecular dynamics simulations at constant pressure using the GROMOS 45a4 united atom forcefield. To test the forcefield, we computed the density, thermal expansion coefficient, total dipole moment, and dielectric constant of cellulose Iβ, finding broad agreement with experimental results. We computed infrared (IR) spectra of cellulose Iβ over the range 300–550 K as a probe of hydrogen bonding. Computed IR spectra were found to agree semi-quantitatively with experiment, especially in the O–H stretching region. We assigned O–H stretches using a novel synthesis of normal mode analysis and power spectrum methods. Simulated IR spectra at elevated temperatures suggest a structural transformation above 450 K, a result in agreement with experimental IR results. The low-temperature (300–400 K) structure of cellulose Iβ is dominated by intrachain hydrogen bonds, whereas in the high-temperature structure (450–550 K), many of these transform to longer, weaker interchain hydrogen bonds. A three-dimensional hydrogen bonding network emerges at high temperatures due to formation of new interchain hydrogen bonds, which may explain the stability of the cellulose structure at such high temperatures. © *2011 American Institute of Physics*. [doi:10.1063/1.3646306]

I. INTRODUCTION

Energy from biomass is one of the possible sustainable sources of clean fuels.[1–3] Pyrolysis is one of the most promising routes for converting lignocellulosic biomass to biofuels.[4,5] Pyrolysis involves thermal decomposition usually in the absence of oxygen.[6–8] Although pyrolysis has been studied for over 60 years, the reaction mechanism(s) at the molecular level are still not well understood. Cellulose comprises more than half of plant material and, thus, is the most abundant biomolecule on earth.[9] As such, molecular understanding of cellulose pyrolysis is important in developing efficient technologies for the conversion of biomass. In this article, we apply molecular dynamics to investigate structures and vibrational signatures of cellulose at elevated temperatures.

There are two broad sets of understanding in the literature about the mechanism of cellulose pyrolysis. Several reports assert that cellulose pyrolyses to solid, liquid, and gaseous products through an "active cellulose" intermediate,[10–16] while other reports assume that no such intermediate exists.[17–21] Of the mechanisms that include active cellulose, some postulate that active cellulose arises from irreversible depolymerization yielding a liquid above 550 K,[12,22–24] while others suggest active cellulose forms reversibly below 550 K from conformational changes in the solid.[15,16] Because of this level of controversy, we have studied the molecular structure and dynamics of cellulose at elevated temperatures to search for structural transitions. In particular, we have modeled cellulose Iβ up to 550 K using classical molecular dynamics to compute the infrared (IR) spectrum as a probe of hydrogen bonding. This work is a first step to gain molecular-level understanding of the mechanism of cellulose pyrolysis. In future work, we will model cellulose depolymerization at much higher temperatures using reactive dynamics methods.

Cellulose is synthesized in the plasma membrane of plant cells during biogenesis in the form of highly crystalline microfibrils.[25] The primary structure of cellulose is a linear homopolymer of glucose residues in the D-configuration and connected by β-(1–4) glycosidic linkages as shown in Fig. 1.[9] Free hydroxyl groups present in cellulose are involved in various possible intramolecular and intermolecular hydrogen bonds giving rise to different crystalline arrangements of cellulose. Cellulose has four principal polymorphs: I, II, III, and IV.[9] Naturally occurring (native) cellulose is cellulose I, the most abundant organic polymer on the earth. Cellulose I has been found to be a mixture of two crystalline forms, Iα and Iβ, present in statistically different proportions.[26] Both these structures consist of cellulose chains with alternate glucose units facing in opposite directions. These chains are arranged in parallel fashion and are linked through interchain OH···H hydrogen bonds. Sheets of polymeric chains are stacked over one another, stabilized by weaker CH···O interactions and van der Waals attractions.[27,28] Cellulose Iβ is the dominant form present in most higher plant material,

[a)]Electronic mail: vagarwal@ecs.umass.edu.
[b)]Electronic mail: huber@ecs.umass.edu.
[c)]Electronic mail: wconner@ecs.umass.edu.
[d)]Electronic mail: auerbach@chem.umass.edu.

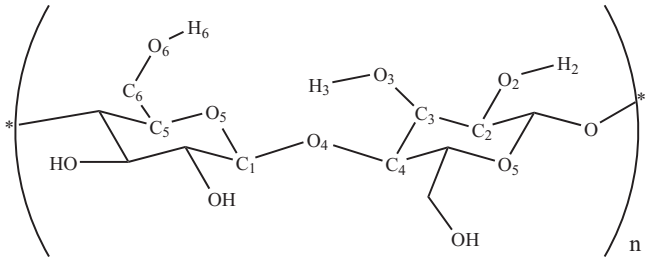

FIG. 1. Schematic representation of the cellulose repeat unit.

prompting us to model the thermophysical properties of cellulose Iβ in the present study.

In their study of cellulose pyrolysis, Lin *et al.*[15] found a reversible heat gain without mass loss at 475 K, suggestive of forming active cellulose. Wada studied structural changes in cellulose Iβ upon heating using x-ray diffraction,[29,30] finding an increase in the *a* parameter and a sudden decrease in the *b* parameter above 490 K, suggesting formation of a high temperature phase above 490 K. Watanabe *et al.*[31,32] reported IR spectra that support the conclusions above. They interpreted the temperature-dependence of their IR spectra by positing a gradual disruption of intrachain hydrogen bonds between 300–470 K, followed by a sudden collapse of intrachain hydrogen bonds and formation of a new structure with weaker hydrogen bonds around 490 K.

Molecular modeling studies performed by Bergenstråhle *et al.*[33] have also suggested a structural change above 450 K. In a more recent study, Matthews *et al.*[34] have studied the structural changes in cellulose mircrofibrils at high temperatures in a hydrated environment. They found that twisting between neighboring sheets ceases due to the changes in hydrogen bonding at high temperatures. However, no study has been performed to compute the IR spectrum of cellulose as a probe of hydrogen bonding for comparison with experiment. Moreover, the interpretation suggested by Watanabe *et al.*[31,32] is based on the spectral assignments postulated by Maréchal and Chanzy,[35] which need to be tested by computer simulations. Using molecular dynamics to compute the dipole moment correlation function, one can obtain the IR spectrum taking into account anharmonicity and mode coupling present in many hydrogen-bonded systems. The challenge then becomes assigning peaks in the computed IR spectra. The presence of anharmonicity limits the use of normal mode analysis (NMA) (Refs. 36 and 37) for assigning peaks because the results depend too much on the configuration used for calculating second derivatives. Van Houteghem *et al.*[38] have recently proposed a new method for interpreting vibrational spectra by projecting atomic velocities on selected directions of internal modes. However, the formulation of this method has been closely tied to vibrations in zeolite systems and, hence, may be of limited utility for our present study. Other approaches such as effective normal mode analysis[39] and principle mode analysis[40] have been reported for interpreting condensed-phase vibrational spectra, but these methods are largely relegated to analyzing liquids. To assign the IR spectra of cellulose Iβ at various temperatures, we report below a novel synthesis of NMA and power spectrum methods,[41] combined with constant-pressure simulations to account for anharmonicity.

Cael *et al.*[42] have previously applied NMA to cellulose I using a valence forcefield but could not reproduce the various OH stretching modes that arise from different hydrogen bonding patterns in cellulose. In addition, these authors did not test the forcefield by computing cellulose structure and other thermophysical properties. Moreover, this work was performed before the discovery of dimorphism (Iα and Iβ) in native cellulose. To address these issues, we have performed classical molecular dynamics simulations to compute IR spectra of cellulose Iβ as a probe of hydrogen bonding to understand effects from elevated temperature. We have used the GROMOS forcefield,[43] which includes a quartic function to describe bond stretches. Our approach for assigning IR peaks takes into account the anharmonicity present in the forcefield.

We find below that most of our assignments in the OH stretching region agree well with previous results. However, we have found that some assignments need to be revisited. We find a structural transition of cellulose above 450 K due to disruption of intrachain hydrogen bonds, leading to formation of weaker interchain hydrogen bonds. We find a featureless IR spectrum above 450 K in agreement with experiment. However, in contrast to previous results which explain this featureless spectrum by positing disruption of OH3$\cdots$O5 hydrogen bonds, we find no such disruption in our simulations. We elaborate on this and other new findings below.

The remainder of this article is organized as follows: in Sec. II, we describe the methods for computing physical properties and IR spectra of cellulose Iβ, followed by the new approach for assigning peaks in the IR spectra, in Sec. III, we give results and discussion of the IR spectra and hydrogen bonding patterns of cellulose at various temperatures, and in Sec. IV, we offer concluding remarks.

II. METHODOLOGY

A. Model

Cellulose Iβ has a monoclinic unit cell [a = 7.784 Å, b = 8.201 Å, and c = 10.38 Å; γ = 96.5°] with a space group of $P2_1$.[44] The simulation box used in this study consisted of 4 × 4 × 4 primitive unit cells (5888 total atoms, 3584 united atoms) of cellulose Iβ; a total of 256 glucose units arranged in 32 chains of length 8 glucose units. A detailed picture of the simulation cell is shown in Fig. 2. We observed no change in the average thermophysical properties (see Sec. III A) as well as the peaks of the computed IR spectrum (see supplementary material[45]) upon increasing the system size to 5 × 5 × 5 unit cells. For computational efficiency, only polar hydrogens were treated explicitly, with non-polar hydrogens treated as united atoms with the corresponding bonded atom. As such, CH and CH_2 groups were treated as united atoms with distinct atom types, masses, and interaction parameters. We also performed vibrational analysis of glucose to see whether coupling is present between the high frequency C–H and O–H stretching modes (see supplementary material[45]), using B3LYP/6-311G(d,p) level of theory in GAUSSIAN03.[46] We found no coupling between the

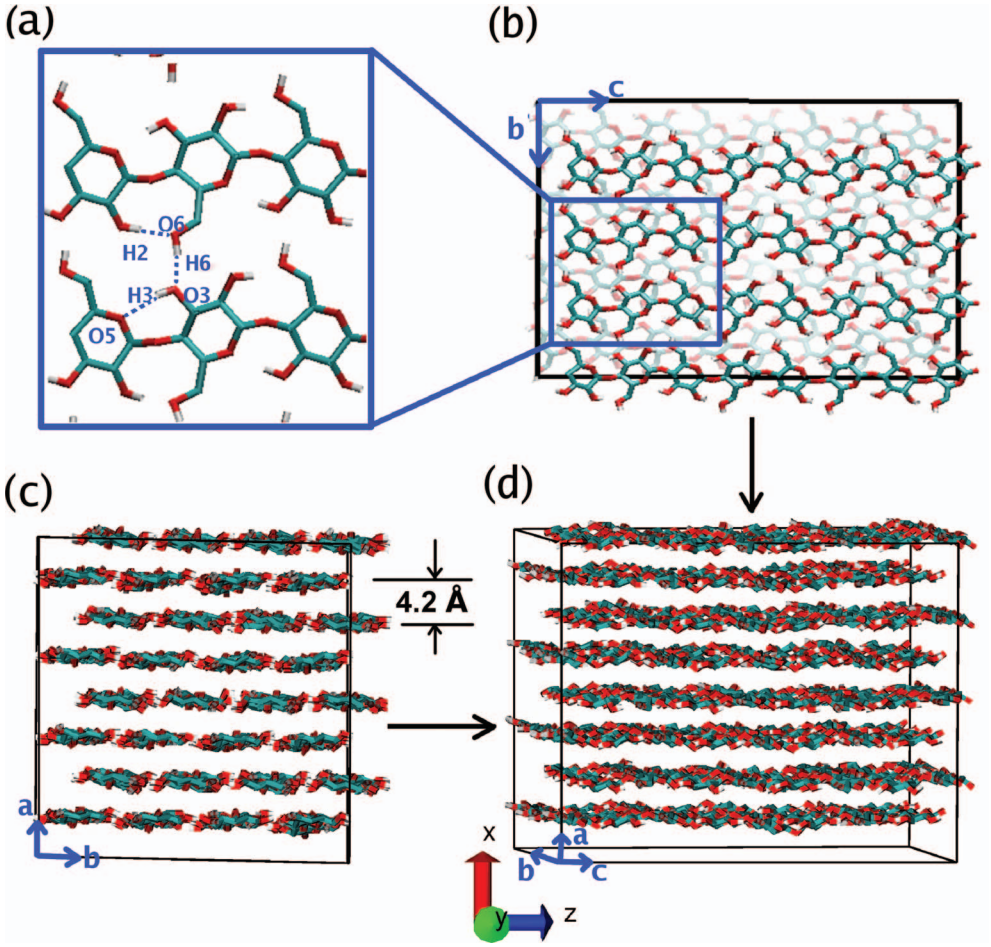

FIG. 2. Equilibrated structure of cellulose Iβ at 300 K. (a) Representation of different hydrogen bonds in the bc plane. (b) View along unit cell a. (c) View along unit cell c. (d) Three-dimensional view of the unit cell.

C–H and O–H stretching modes, likely because of the 500 cm^{-1} mismatch. Hence, the use of this united atom model does not affect the O–H stretching modes, which are the focus of our work.

The initial coordinates were obtained from previous experimentally determined x-ray and neutron diffraction studies,[44] which showed the presence of two different hydrogen bonding patterns in pure crystalline cellulose Iβ, corresponding to major and minor conformations. The difference was attributed to the multiple geometries of O6H6 and O2H2 hydrogen atoms. It has been shown previously that the minor conformation is energetically unfavorable,[28,47] and believed to be the crystallographic average of a number of possible disordered hydrogen bonding patterns within the crystal.[28] For the present study, the hydrogen bonding pattern corresponding to the major conformation was used for constructing initial conditions for molecular dynamics.

B. MD simulations

Atomistic molecular dynamics (MD) simulations were performed using the GROMACS 4.07 simulation package.[48] The united atom forcefield GROMOS 45a4,[49] developed for hexapyranose-based carbohydrates, was used for this study of cellulose structure and dynamics. A previous study comparing 18 different forcefields has shown that GROMOS, GLYCAM06, and MM3 are the best choices for studying disaccharides such as cellobiose.[50] It was also shown previously that the GROMOS 45a4 forcefield reproduces the crystal structure of cellulose Iβ at room temperature.[33] We have used the GROMOS forcefield since it allows a computationally balanced approach by representing the OH groups explicitly, and the CH groups as united atoms. GROMOS 45a4 estimates bond-stretch potential energies using an anharmonic quartic potential as[43,51]

$$V_b = \frac{1}{4} k_b \left[\vec{r}_{ij} \cdot \vec{r}_{ij} - r_0^2 \right]^2, \tag{1}$$

where k_b is the quartic force constant, r_0 is the equilibrium bond length, and $\vec{r}_{ij}$ is the distance vector between the ith and jth atoms. The quartic force constant is related to the harmonic force constant (denoted as "k_b^{harm}") according to[51]

$$k_b = \frac{k_b^{\text{harm}}}{2r_0^2}. \tag{2}$$

Since the harmonic force constant is proportional to the square of the wavenumber, Eq. (2) suggests that the quartic force constant is also proportional to the square of the wavenumber. To fit the experimentally measured[35] O6–H6

vibrational frequency, the H-OA quartic force constant was adjusted from 1570 to 1750 kJ/mol/Å^4.

Periodic boundary conditions were applied in all directions according to the minimum image convention[52,53] to mimic an infinite crystal. Short range interactions were computed using a Lennard-Jones potential, with a dispersion correction of both energy and pressure using a cutoff of 12 Å. Neighbor lists for non-bonded interactions were generated every time step using the cut-off radius of 12 Å. Coulombic interactions were calculated with an electrostatic cutoff of 12 Å using the Particle-mesh Ewald method[54] with a Fourier grid spacing of 1.2 Å and an interpolation order of 4. The leap frog algorithm[52] was used to integrate Newton's equations of motion using a time step of 1.0 fs.

IR spectra were computed by performing constant-volume (NVT) MD simulations with target temperatures of 300, 350, 400, 450, 500, and 550 K. To generate an initial equilibrated structure at each temperature, constant-pressure (NPT) MD simulations were performed for 5 ns at each temperature with a target pressure of 1 bar. We observed no structural change for the next 5 ns. The data collected during this run was used to compute the thermophysical properties such as cell parameters, density, and thermal expansion coefficients. In general, velocities were randomly initialized using a Maxwellian distribution at the target temperature. The temperature of the system was kept constant using the Nosé-Hoover[55–57] thermostat with a time coupling parameter of 0.1 ps. We found that increasing this time coupling parameter had no significant effect on IR peak positions nor on the average temperature. NVT MD simulations were performed for 350 ps and the average properties were computed for the last 250 ps with data collected at every 4 fs (see Sec. II E for more details on the IR spectra calculations). The electrical flux-flux correlation function used to calculate the IR spectrum was found to decay in a time scale of picoseconds (see supplementary material[45] for the 300 K correlation function). This suggests a simulation time of 250 ps is enough to the calculate IR spectrum. For NPT simulations, the pressure was controlled using an anisotropic Berendsen barostat[58] with a coupling parameter of 1 ps. The target pressure was set to 1 bar along the diagonal xx, yy, and zz directions, and to 0 bar along the off-diagonal xy/yx, xz/zx, and yz/zy directions. The compressibility was set to 10^{-6} bar^{-1} in all directions, and the reference coordinates were scaled with the scaling matrix of the pressure coupling.[48]

Hydrogen bonds were counted using a cut-off distance of 2.5 Å between a hydrogen and its acceptor oxygen. We found no change in the trends of hydrogen bonding upon changing the cut-off distance by ±0.1Å.

C. Thermal expansion coefficient

Thermal expansion coefficients were calculated for the unit cell dimensions a and b at 300 and 500 K. The cell parameters were obtained by performing NPT simulations for 10 ns and the average lattice parameters were obtained from the last 5 ns. The average lattice parameters were computed for the temperature ranges of 280–320 K and 480–520 K. Two linear least square fits were performed separately in these temperature ranges. The slopes obtained from these fits were used to calculate the thermal expansion coefficients as follows:

$$\alpha = \frac{1}{l_{T=273}} \frac{dl}{dT}, \tag{3}$$

where α is the thermal expansion coefficient, l is the unit cell length in a or b directions, and T is the temperature of the system.

D. Dipole moment and dielectric constant

The total dipole moment [denoted as $M(t)$] of the cellulose simulation cell at any time t was obtained by summing the product of charges and position vectors of the individual atoms as

$$M(t) = \sum_{i=1}^{N} q_i \vec{r}_i, \tag{4}$$

where N is the total number of atoms and q_i is the charge and $\vec{r}_i$ is the position vector of the ith atom. The (relative) dielectric constant (denoted as ε) of a material can be written in terms of real and imaginary parts according to[59]

$$\varepsilon(\omega) = \varepsilon'(\omega) - i\varepsilon''(\omega), \tag{5}$$

where $\varepsilon'(\omega)$ is the frequency-dependent dielectric constant associated with polarization, $\varepsilon''(\omega)$ is the frequency-dependent dielectric constant associated with heating ("loss"), and ω is the angular frequency. In the limit $\omega \to 0$, one finds that $\varepsilon'' \to 0$ and ε' becomes the static dielectric constant (e.g., ~80 for water at STP). We calculated the static dielectric constant of cellulose Iβ using the Debye dielectric theory,[59] which assumes exponential decay of the total dipole moment correlation function with time constant τ, hence giving the following equations for $\varepsilon'(\omega)$ and $\varepsilon''(\omega)$:

$$\varepsilon'(\omega) = 1 + 4\pi\beta\sigma_M^2 \left(\frac{1}{1+\omega^2\tau^2}\right), \tag{6}$$

$$\varepsilon'(0) = 1 + 4\pi\beta\sigma_M^2, \tag{7}$$

$$\varepsilon''(\omega) = 4\pi\beta\sigma_M^2 \left(\frac{\omega\tau}{1+\omega^2\tau^2}\right), \tag{8}$$

where $\sigma_M^2 = \langle \delta\vec{M}(0)\delta\vec{M}(0)\rangle$ is the variance of the total dipole moment because of thermal fluctuations.

E. Infrared spectrum

The infrared spectrum for a system in equilibrium can be computed using linear response theory[59,60] by Fourier transforming the total dipole moment autocorrelation function[36,61] as:

$$\begin{aligned} I(\omega)_{cl} &= \frac{1}{2\pi}\int_{-\infty}^{\infty} dt\ e^{-i\omega t}\langle \delta\vec{M}(0)\cdot\delta\vec{M}(t)\rangle \\ &= \frac{1}{2\pi}\int_{-\infty}^{\infty} dt\ e^{-i\omega t}\{\langle \vec{M}(0)\cdot\vec{M}(t)\rangle - |\langle\vec{M}\rangle|^2\}, \end{aligned} \tag{9}$$

where $I(\omega)_{cl}$ is the classical spectral density or the classical absorption lineshape and ω is the angular frequency of the

IR radiation. Using periodic boundary conditions during MD simulations causes discontinuities in position due to leaving and entering of atoms inside the simulation box.[62] By using Parseval's theorem,[59] the Wiener-Khintchine theorem,[59] and properties of Fourier transforms,[63] several authors have shown that $I(\omega)_{cl}$ can be converted to a mathematically equivalent form[62,64,65]

$$I(\omega)_{cl} = \frac{1}{2\pi\omega^2}\int_{-\infty}^{\infty} dt\; e^{-i\omega t}\left\langle \frac{d\vec{M}(0)}{dt}\cdot\frac{d\vec{M}(t)}{dt}\right\rangle = \frac{1}{2\pi\omega^2}\int_{-\infty}^{\infty} dt\; e^{-i\omega t}\left\langle\left(\sum_{i=1}^{n} q_i\vec{v}_i(0)\right)\cdot\left(\sum_{j=1}^{n} q_j\vec{v}_j(t)\right)\right\rangle, \tag{10}$$

where $\vec{v}_i(t)$ is the velocity of ith particle at time t. The quantity $\langle(\sum_{i=1}^{n} q_i\vec{v}_i(0))\cdot(\sum_{j=1}^{n} q_j\vec{v}_j(t))\rangle$ is referred to as the electrical flux-flux correlation function. Casting the spectrum in terms of the velocities avoids the problem with periodic boundary conditions.

To prevent spectral leakage due to non-periodic data, the Blackman window[66–68] was applied as a data filter before applying the Fourier transform. The resulting IR spectra were smoothed using a 9-point moving average filter[69] to reduce spectral noise. To correct the spectral density obtained from the classical correlation function, several quantum correction factors have been suggested in the literature.[37,70] The quantum correction factor based on the "harmonic approximation" (HA) (Refs. 37 and 70) was applied in this study; this factor has previously been shown to work best for hydrogen bonded systems.[37] The corrections based on HA become significant at high frequencies and low temperatures (for T = 300 K and $\bar{\nu}$ = 3500 cm^{-1}, HA = 16.8; for T = 300 K and $\bar{\nu}$ = 500 cm^{-1}, HA = 2.7; at T = 550 K and $\bar{\nu}$ = 3500 cm^{-1}, HA = 9.2). The final spectral density is obtained as follows:

$$I(\omega) = Q_{\mathrm{HA}} I(\omega)_{cl} = \left(\frac{\beta\hbar\omega}{1-\exp(-\beta\hbar\omega)}\right)\frac{1}{2\pi\omega^2}\int_{-\infty}^{\infty} dt\; e^{-i\omega t}\left\langle \frac{d\vec{M}(0)}{dt}\frac{d\vec{M}(t)}{dt}\right\rangle. \tag{11}$$

F. Assignment of peaks

The following approach was used for assigning peaks in the IR spectrum, with a focus on the OH stretching region:

- IR spectra at various temperatures were computed.
- For a particular temperature, the normal mode spectrum was obtained as outlined below. The normal mode frequencies correspond to all the vibrational modes of the system, some of which are IR inactive.
- For each normal mode in the OH stretching region of the normal mode spectrum, the atom exhibiting the maximum displacement in the corresponding eigenvector was identified.
- The power spectrum for this atom was then computed as outlined below at the appropriate temperature. This allows a local assignment of the IR spectrum, while incorporating anharmonicity from the quartic forcefield in the power spectrum.
- The peak in the IR spectrum with maximal overlap with the main peak in the power spectrum was thus assigned to the motion of the corresponding atom (or OH bond).

G. Normal mode analysis

In NMA, cellulose Iβ is considered to be a $3N$-dimensional harmonic oscillator, where N = 3584 atoms in the simulation cell under periodic boundary conditions. The instantaneous configuration of cellulose in Cartesian space is denoted by the $3N$-dimensional vector $\vec{r}^N = (\vec{r}_1, \vec{r}_2, \vec{r}_3, \ldots, \vec{r}_N)$, where $\vec{r}_i$ is the three-dimensional position vector of the ith atom. Similarly, the ground-state configuration in Cartesian space is denoted by $\vec{r}_0^N = (\vec{r}_1^{(0)}, \vec{r}_2^{(0)}, \vec{r}_3^{(0)}, \ldots, \vec{r}_N^{(0)})$. This ground state depends on the lattice parameters (a, b, c), which in turn depend on temperature because of anharmonicity (see Fig. 2). Furthermore, a Cartesian displacement in the ground state is denoted by $\Delta\vec{r}^N = \vec{r}^N - \vec{r}_0^N = (\Delta\vec{r}_1, \Delta\vec{r}_2, \Delta\vec{r}_3, \ldots, \Delta\vec{r}_N)$. Finally, the displacement in mass-weighted Cartesian space is $\vec{q}^N = (\sqrt{m_1}\Delta\vec{r}_1, \sqrt{m_2}\Delta\vec{r}_2, \sqrt{m_3}\Delta\vec{r}_3, \ldots, \sqrt{m_N}\Delta\vec{r}_N) = (\vec{q}_1, \vec{q}_2, \vec{q}_3, \ldots, \vec{q}_N)$. Using these definitions, the harmonic approximation for the potential energy in Cartesian space is given by

$$V(\Delta\vec{r}^N) \cong V(\vec{0}) + \frac{1}{2}\sum_{i=1}^{N}\sum_{j=1}^{N}\left(\frac{\partial^2 V}{\partial(\Delta\vec{r}_i)\partial(\Delta\vec{r}_j)}\right)_{\vec{0}} : \Delta\vec{r}_j\Delta\vec{r}_i, \tag{12}$$

and in mass-weighted Cartesian space is given by

$$V(\vec{q}^N) \cong V(\vec{0}) + \frac{1}{2}\sum_{i=1}^{N}\sum_{j=1}^{N}(\vec{\nabla}_i\vec{\nabla}_j V)_{\vec{0}} : \vec{q}_j\vec{q}_i. \tag{13}$$

In Eq. (13), $(\vec{\nabla}_i\vec{\nabla}_j V)_{\vec{0}}$ is a 3×3 mass-weighted force constant matrix[71] evaluated at a temperature-dependent ground state configuration of cellulose. For each temperature, average cell parameters were computed by performing NPT equilibration runs as mentioned in Sec. II B. These cell parameters were then fixed to their average values for a given temperature, and the system potential energy was minimized using the conjugate gradient method[72,73] until the root-mean-square forces were less than 0.001 eV/Å. The resulting structure was used to obtain the force constant matrix. Normal modes were computed by calculating the eigenvalues and eigenvectors of the $3N\times 3N$ mass-weighted force constant matrix $[A_{ij}]_{N\times N}$ (where $A_{ij} = (\vec{\nabla}_i\vec{\nabla}_j V)_{\vec{0}}$),[74] using standard routines implemented in GROMACS utilities.[48] Of the $3N$ eigenvalues (k_i) so obtained, the first six equal zero corresponding to the three translational and three rotational motions, while the remaining $3N-6$ eigenvalues correspond to all the vibrational modes which may or may not be IR active. The wavenumber corresponding to the ith normal mode is given by $\bar{\nu}_i = \sqrt{k_i/4\pi^2c^2}$, where c is the speed of light. The normal mode spectrum was obtained by plotting Lorentzian functions

centered on the NMA wavenumbers ($\bar{\nu}_i$) according to

$$I(\bar{\nu}) = \sum_i \frac{\Gamma}{(\Gamma^2 + (\bar{\nu} - \bar{\nu}_i)^2)}, \quad (14)$$

where Γ is a Lorentzian linewidth taken to be 1 cm^{-1}, and the normal mode spectrum was plotted using a binwidth in $\bar{\nu}$ of 1 cm^{-1}.

To assist in the IR assignments, we generated visualizations of various normal mode vibrations of cellulose Iβ. The eigenvectors ($\vec{U}_i$) obtained represent displacement directions of the normal modes in mass-weighted Cartesian space. The normal mode directional vectors ($\vec{u}_i$) in Cartesian space can be obtained from $\vec{U}_i$ by dividing with the square root of mass of the ith atom and then re-normalizing the resulting vector. Motion in Cartesian space along a given normal mode is obtained by

$$\vec{r}^N = \vec{r}_0^N \pm \lambda \vec{u}_i, \quad (15)$$

where λ is the fractional displacement along the normal mode vector.

H. Power spectrum

Because of the anharmonicity in the GROMOS 45a4 forcefield (see Eq. (1)), normal mode frequencies are often shifted from IR peak positions. To link the normal mode results with the computed IR spectra, we computed power spectra of selected atoms using the selection algorithm described above. Power spectra were obtained by computing Fourier transforms of atomic velocity autocorrelation functions according to[39]

$$I(\omega)_{pw} = \frac{1}{2\pi} \int_{-\infty}^{\infty} dt\ e^{-i\omega t} \langle \delta \vec{v}_i(0) \delta \vec{v}_i(t) \rangle, \quad (16)$$

where v_i is the velocity vector of the ith atom.

III. RESULTS AND DISCUSSION

We begin by presenting calculations of thermophysical properties to test the performance of the GROMOS 45a4 forcefield. We then present the IR spectrum of cellulose Iβ at room temperature, and our assignment of its peaks with special focus on the OH stretching region. Finally, we present the temperature dependence of the IR spectrum and the hydrogen bonding pattern of cellulose.

A. Thermal expansion of cellulose at standard pressure

We calculated the density variation with temperature and thermal expansion coefficients at 300 and 500 K. Figures 2 and 3 show various aspects of low- and high-temperature structures of cellulose Iβ, respectively. Here we focus on Figs. 2(c) and 3(c), which show the intersheet spacing increase from 4.2 to 4.4 Å, from 300 to 500 K. This accounts for the change in density discussed below. We reference

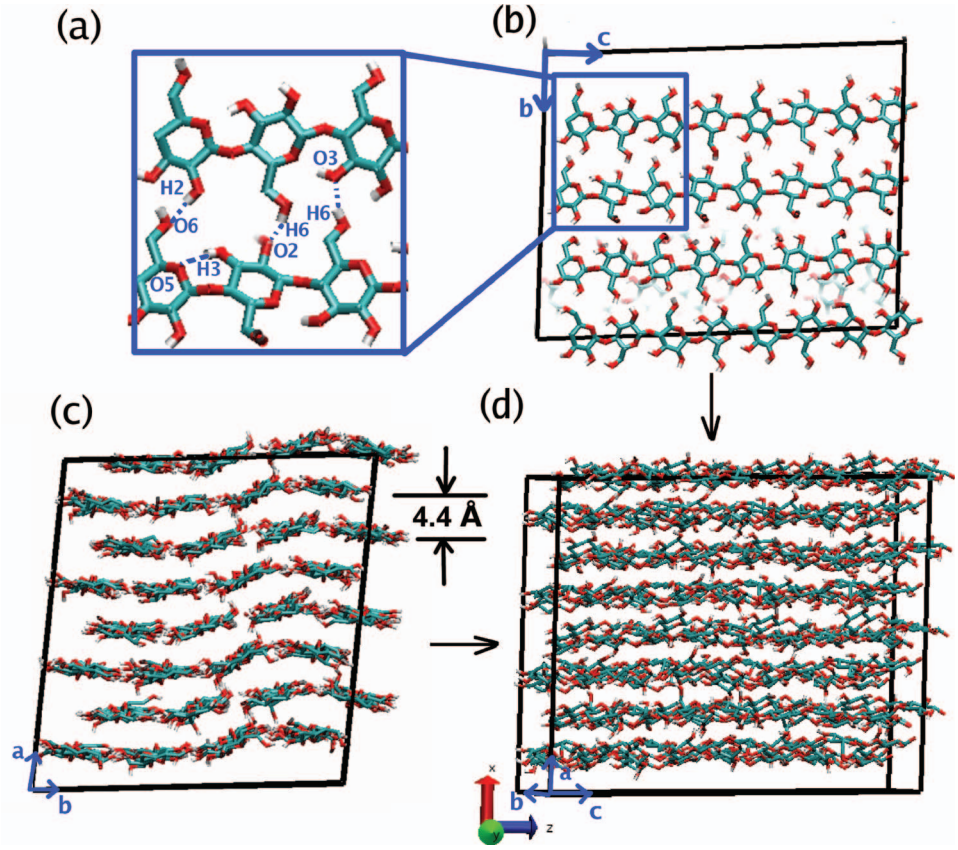

FIG. 3. Equilibrated structure of cellulose Iβ at 500 K. (a) Representation of different hydrogen bonds in the bc plane. (b) View along unit cell a. (c) View along unit cell c. (d) Thee-dimensional view of the unit cell.

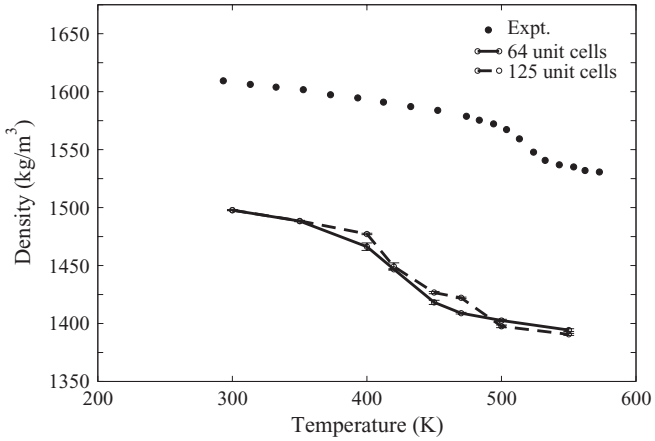

FIG. 4. Computed and experimental[30] variation of density with temperature.

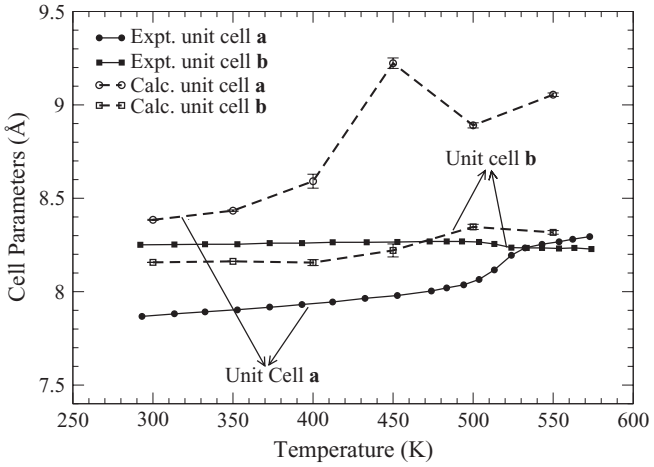

FIG. 5. Variation of cell parameters a and b with temperature. The experimental values were obtained from Wada *et al.*[30]

Figs. 2 and 3 in the analysis and discussion throughout the rest of the paper. We performed these simulations to benchmark our study with the results reported previously by Bergenstråhle *et al.*[33] The average density of cellulose Iβ at 300 ± 4 K was obtained as 1498 ± 0.5 kg/m^3, which is 3% less than that estimated from the experimental studies performed on cellulose Iβ.[44,75,76] This is because the GROMOS 45a4 forcefield overestimates the unit cell *a* parameter (by 8%), the direction perpendicular to the cellulose sheets. As mentioned previously by Bergenstråhle *et al.*,[33] the overestimation of the *a* parameter may be due to the incomplete treatment of intermolecular forces arising from the united atom model, which underestimates carbon negative charges in CH and CH_2 groups, thereby underestimating Coulombic interactions.

The computed and experimental[30] variations of density with temperature are given in Fig. 4, which shows simulation results for 64 and 125 unit cells. The simulated and experimental densities show the same trends, though as mentioned above, our simulations underestimate the density due to overestimation of the *a* parameter. As expected, the density decreases with increasing temperature. There is a sudden decrease in density between 400–450 K in simulations, and around 500 K in experiments, suggesting a marked structural change. Is this structural change were a first-order phase transition, we would see the simulated density change with temperature becomes more precipitous for larger system sizes. This is not the case, as shown in Fig. 4, suggesting that this structural change is indeed not a first-order phase transition.

The computed variations with temperature of the unit cell parameters *a* and *b* are plotted in Fig. 5 along with experimentally obtained unit cell parameters from x-ray diffraction studies performed by Wada *et al.*[30] As mentioned before we observe an overestimation by simulations of the *a* parameter by ∼8%. The experimental results exhibit a monotonic increase in the *a* parameter and a monotonic decrease in the *b* parameter with a possible structural change observed in the temperature range 500–530 K. In contrast, the simulated values do not exhibit monotonic trends. Indeed, the *a* parameter shows a reproducible maximum at 450 K that was also found in the previous study by Bergenstråhle *et al.*[33] This maximum occurs with an approximately balancing minimum in the unit cell angle γ, thereby eliminating a cusp in the density. This effect may have been masked by experimental x-ray results because the sample contained a mixture of major and minor conformations.[28,44,47] More research is needed to determine if this effect is real, and if so, how it can be revealed experimentally.

The simulated thermal expansion coefficients for *a* and *b* cell dimensions are 10.8×10^{-5} and 1.3×10^{-5} K^{-1}, respectively. The corresponding experimental values are 9.8×10^{-5} and 1.2×10^{-5} K^{-1}, respectively.[30] Our calculations overestimate these thermal expansion coefficients by only 12% and 9% for *a* and *b* cell dimensions, respectively, indicating excellent agreement with experimental results at 300 K. At elevated temperatures (>500 K) Wada *et al.*[30] estimated thermal expansion coefficients for unit cell parameters *a* and *b* as 19.8×10^{-5} and -1.6×10^{-5} K^{-1}, respectively. Our simulated thermal expansion coefficients at 500 K are 31.5×10^{-5} and -4.1×10^{-5} K^{-1}, respectively, again showing excellent agreement with experiment in both sign and order of magnitude. The negative thermal expansion coefficient along the y-axis at 500 K was found to arise in our simulations from tilting of cellulose chains as shown in Fig. 3. Comparing the equilibrated structures at 300 K (Fig. 2) and 500 K (Fig. 3) perpendicular to the xy plane, it can be seen that the high-temperature structure has tilted chains. This effect of tilting of chains has also been reported previously.[34,77] We found that at low temperatures (<450 K), most of the O5-C5-C6-O6 torsional angles assume a *trans-gauche* (an angle of 180°) conformation. These convert to *gauche-gauche* (an angle of 300°) and *gauche-trans* (an angle of 60°) conformations at high temperatures (data not shown) similar to the finding previously reported by Bergenstråhle *et al.*[33]

B. Dipole moment and dielectric constant

The total dipole moment of cellulose as a function of time obtained from MD simulations is plotted in Fig. 6. This shows that the major contribution to the overall dipole moment is along the z-axis which is parallel to the cellulose chains. The average dipole moment along the y-axis is found to be 0 ± 0.05 D, which is expected since the cellulose polymer

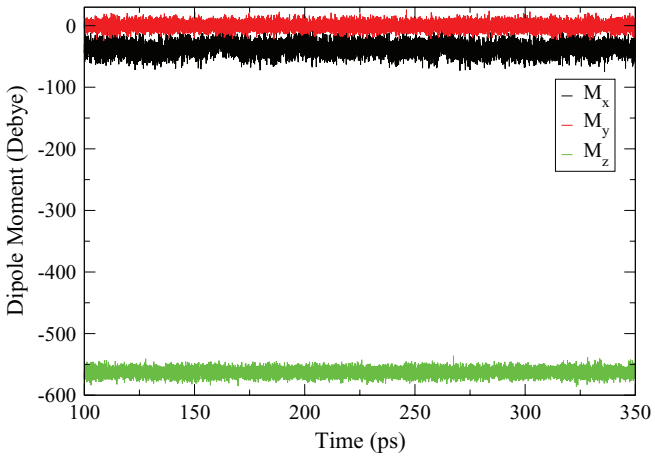

FIG. 6. Total dipole moment of cellulose Iβ simulated at 300 K. The mean components are $\langle M_x \rangle = -37$ D, $\langle M_y \rangle = -0.2$ D, $\langle M_z \rangle = -562.6$ D, and the variance is $\sigma_M^2 = 176$ D^2.

consists of alternating glucose units with 180° flips along the y-axis. The average magnitude of celluloses dipole moment obtained from our calculations is 4.4 D per cellobiose unit. Since cellulose is soluble only under extreme conditions, an experimental value of the total dipole moment of cellulose is not available.[78] Thus, direct comparison to our simulations is not possible. However, dipole moments of cellobiose and derivatives of cellulose have been measured. The dipole moment of cellobiose with a nitrogen content of 12.3% has been reported to be 6.0 D from the dielectric data of Jatkar and Sastry.[79,80] The dipole moment of glucose monomer has been measured for cellulose diacetate in dioxane as 2.8 D (Ref. 81) or 5.6 D per cellobiose unit. Cocinero *et al.* have reported a dipole moment for *o*-phenyl cellobiose of 5.2 and 7.0 D for *trans* and *cis* conformers, respectively, from *ab initio* calculations.[82] Comparing to these values suggests that our simulations provide a reasonable (if somewhat low) estimate of the total dipole moment.

The experimental value of the (relative) static dielectric constant [$\varepsilon'(0)$] of cellulose at 303 K is 2.1.[83] We found from simulation the static dielectric constant to be 1.89 ± 0.01 at 300 ± 4 K, underestimating the experimental value by 10.2%. This low value is consistent with the low dipole discussed above, and may be reflect forcefield error. Alternatively, this may suggest that 90% of the static dielectric response in cellulose arises from reorientation of dipoles (mostly OH groups) with fixed point charges, and that the remainder comes from fluctuating atomic charges (not treated in our model).

The reasonable agreement between our simulations and experiments for the density, thermal expansion coefficients, dipole moment, and dielectric constant at 300 K suggests that the GROMOS 45a4 forcefield provides an adequate representation of the bulk structure and dynamics of cellulose Iβ. Armed with this agreement, we now turn to a study of the IR spectrum at 300 K.

C. IR spectrum of cellulose at 300 K

We show in Fig. 7 the computed IR spectrum of cellulose Iβ at 300 K, alongside the experimental IR spectrum obtained from Maréchal and Chanzy.[35] Before making the comparison, we first summarize the gross assignments of this IR spectrum proposed for cellulose I.[35,84–88] Peaks in the 3000–3600 cm^{-1} band are assigned as O–H stretching modes of the alcoholic groups. The bands located around 2900 cm^{-1} are attributed to the C–H stretching modes; the bands in the 1250–1450 cm^{-1} region are assigned to C–O–H and C–H bending modes; and the bands in the region 950–1250 cm^{-1} are associated with C–O stretching modes.

We now compare the experimental and computed IR spectra of cellulose Iβ. In the region 3000–3600 cm^{-1} we find a good qualitative match in the shape of the IR spectrum, although the computed spectrum is quite a bit more narrow than experiment. This could be because we are using a homogeneous model of cellulose Iβ with only the major conformation,[44] whereas the actual experimental sample contained both conformations and, hence, exhibited heterogeneity in hydrogen bonding.[28,44,47] Moreover, the presence of amorphous regions and moisture in the experimental sample can broaden the IR spectrum in the O–H stretching region.[35] Using NMA and visualizations of the normal modes, we assigned peaks in this region (3000–3600 cm^{-1}) as O–H stretches in agreement with previous interpretations. More detailed assignments of these peaks are provided below in this section.

We observe no computed peak around 2900 cm^{-1}, the putative C–H stretching region, as compared to the experimental spectrum. This is because CH and CH_2 groups are considered as united atoms in the model we have used. This also means that the computed IR spectrum is devoid of other IR-active modes involving CH and/or CH_2 motion, e.g., the CH_2 bend assigned to the experimental peak at 1428 cm^{-1}. Comparing the rest of the IR spectrum with experiment, we observe acceptable agreement in the overall locations of bands, but relatively poor agreement in their intensities. This is likely because of the united atom model, which modifies dipole fluctuations by lumping charges into united atoms.

Maréchal and Chanzy[35] assigned IR peaks in the region 1300–1450 cm^{-1} to C–O–H bending modes. By visualizing normal modes, we have assigned peaks in the 1250–1400 cm^{-1} region to C–O–H bends, suggesting good agreement with experiment with a simulation error (redshift) of 50 cm^{-1}. We were unable to assign the rest of the spectrum below 1250 cm^{-1} due to the delocalized nature of these low-frequency normal modes in cellulose. Because the structure of cellulose is largely controlled by hydrogen bonding mediated by OH groups, the remainder of this paper focuses on the assignment and temperature dependence of the high-frequency O–H stretch region of the IR spectrum.

In the computed O–H stretching region, we find three peaks at 3409, 3366, and 3356 cm^{-1}. A pictorial representation of different types of hydrogen bonds observed at room temperature is given in Fig. 2. We observed no intersheet hydrogen bond at this temperature, giving hydrogen-bonding pattern that is two-dimensional as shown in Fig. 2. The methodology for assignment of these peaks is depicted in Fig. 8. We first computed the NMA spectrum, shown on the x-axis in Fig. 8. We observe an overall blueshift in the IR spectrum in comparison to the NMA spectrum; this shift arises

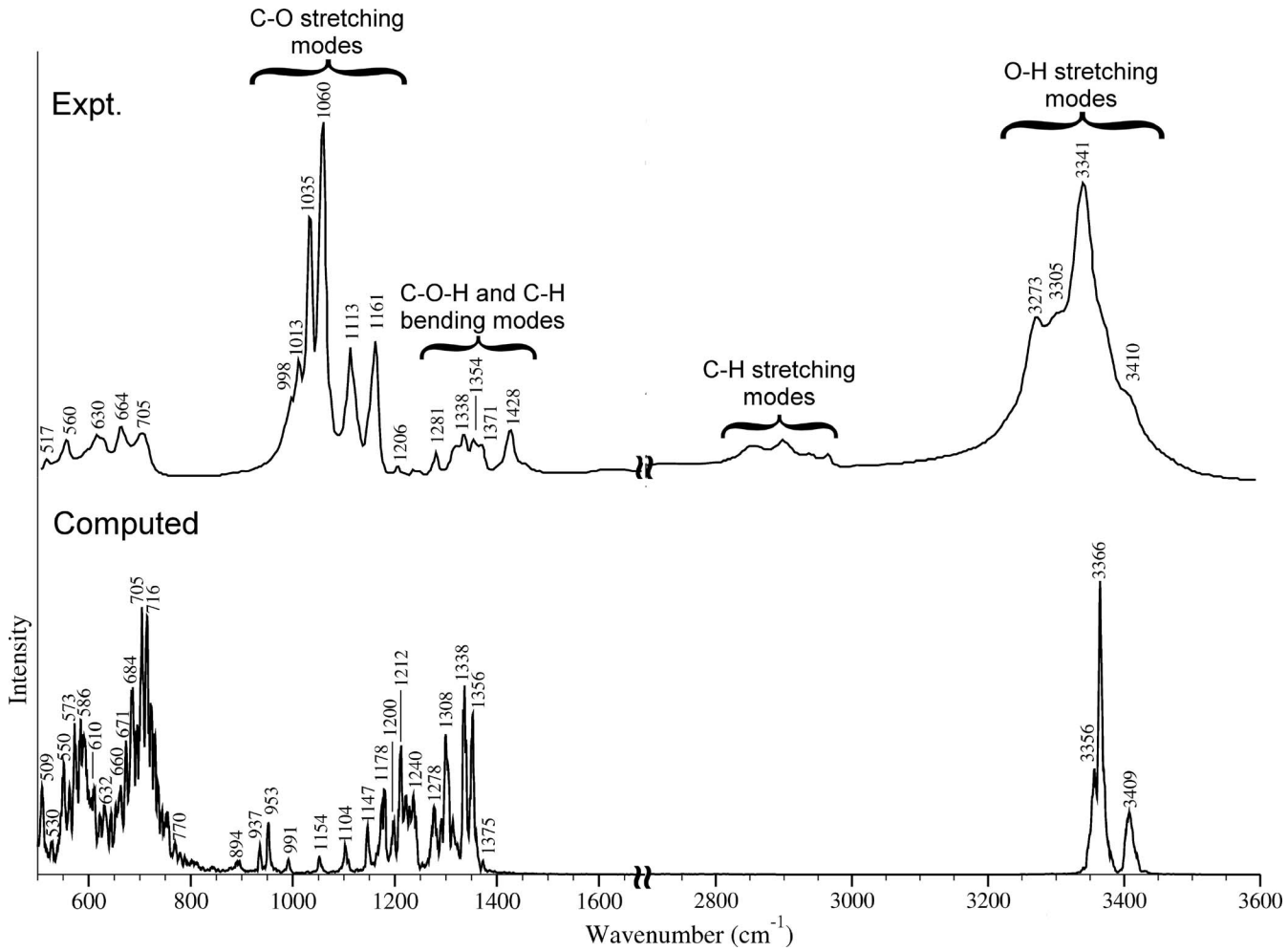

FIG. 7. Computed and experimental[35] IR spectrum of cellulose Iβ at 300 K.

from anharmonicity in the GROMOS 45a4 forcefield. We then analyzed the normal modes corresponding to the peaks in this NMA spectrum, by identifying the atom with maximum displacement for each of the normal mode eigenvectors represented in this spectrum. For example, the NMA spectral peak at 3370 cm^{-1} corresponds to atom number 3174, a hydrogen bound to oxygen O6; this H6 atom represents 78% of the normal mode displacement. We then computed the power spectrum of this atom at the relevant temperature. The wavenumber corresponding to the maximum-intensity peak in the power spectrum of atom 3174 is plotted in Fig. 8 as a dot labeled O6H6$_{3174}$(78). The x-coordinate of this point is the wavenumber from NMA, while the y-coordinate is the wavenumber from the power spectrum; they differ because of anharmonicity in the forcefield. We see from Fig. 8 that the IR peak at 3409 cm^{-1} (y-axis) can be assigned as an O6–H6 stretching mode, which agrees well with the assignment made by Maréchal and Chanzy.[35]

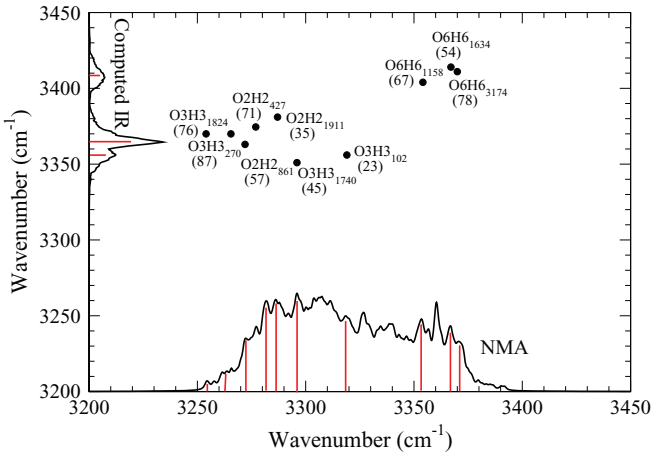

FIG. 8. Normal mode spectrum (x-axis) vs. the computed IR spectrum (y-axis), both in OH stretching region. Dots are locations of main power spectrum peaks, which link normal modes to IR features. Subscripts label hydrogens, and numbers in parentheses give the % displacement in corresponding normal modes.

We also see from Fig. 8 that the assignments of peaks at 3366 and 3356 cm^{-1} are not straightforward because of overlapping O3–H3 and O2–H2 stretching modes. We can, however, gain insight into the relative intensities of these IR peaks by considering hydrogen bonding. In general, stronger hydrogen bonding produces more intense and more redshifted IR peaks, due to flattening of the O–H stretch potential and increased vibrational amplitude.[89] We observe in the simulated IR spectrum more intense peaks at 3356 and 3366 cm^{-1},

redshifted from the less intense peak at 3409 cm^{-1}. Our assignment approach depicted in Fig. 8 suggests that these more intense, redshifted IR peaks involve O2H2 and O3H3 groups. This is consistent with the fact that O2H2 and O3H3 participate in intrachain hydrogen bonding, which is typically stronger in cellulose than the interchain hydrogen bonding of O6H6.

Maréchal and Chanzy[35] have assigned the peak at 3341 cm^{-1} to the O3–H3 stretching mode and the peak at 3273 cm^{-1} to the O2–H2 stretching mode. Our computational results in Fig. 8 suggest, however, that such a clean assignment misses the overlapping nature of O2–H2 and O3–H3 vibrations. Maréchal and Chanzy also argued that only 30% of O2H2 atoms are involved in strong intramolecular hydrogen bonds with O6 atoms, thereby suggesting that only 30% of the O5-C5-C6-O6 torsional angles assume a *trans-gauche* conformation (an angle of 180°). This contradicts results from x-ray diffraction[44] and solid state ^{13}C NMR spectroscopy,[90] which have found that most of the O5-C5-C6-O6 angles are indeed present in *trans-gauche* conformations. This analysis taken together with our modeling results suggest that there is room for new understanding in the assignment of the cellulose Iβ IR spectrum.

D. IR spectrum of cellulose with heating

In Figs. 9 and 10, we show the high-frequency regions of simulated IR spectra of cellulose Iβ in the ranges of 300–400 K and 450–550 K, respectively. We see distinct peaks in the IR spectrum at and below 400 K, while at and above 450 K the spectrum is much more diffuse without discernible features. Such a transition is also seen in the experimental spectra reported by Watanabe *et al.*,[32] where a featureless IR spectrum was observed upon heating. Our simulations suggest two distinct causes of this broadening: redistribution of hydrogen bonds upon heating from 400 K to 450 K, and inhomogeneous broadening even for hydrogen bonds that persist upon heating. Detailed analyses of both these effects are given in Sec. III E. Pictorial representations of the different hydrogen bonds present in the low-temperature and high-temperature structures are also shown in Figs. 2 and 3, respectively.

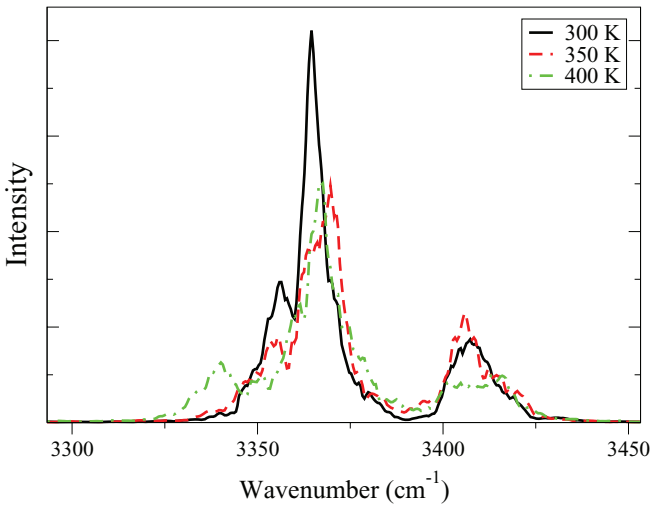

FIG. 9. Computed IR spectrum of cellulose Iβ in temperature range 300–400 K.

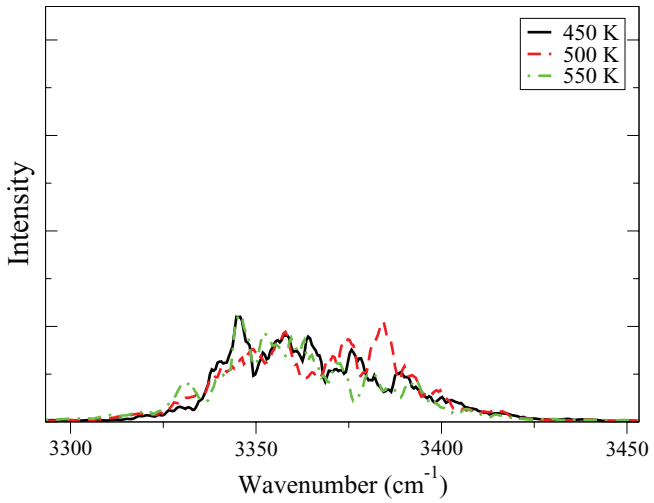

FIG. 10. Computed IR spectrum of cellulose Iβ in temperature range 450–550 K.

In Fig. 9 we find that increasing temperature decreases the intensities of most of the OH peaks. This is because heating weakens hydrogen bonds which tighten OH vibrations, thereby reducing vibrational amplitudes and, hence, oscillator strengths. As temperature increases, the experimental IR peaks in the OH region mostly shift to the blue, in some cases by as much as 1.5%, but mostly by much less.[32] In contrast, our simulations predict very light redshifts upon heating, which remain to be understood.

E. Hydrogen bonding analysis

We show in Fig. 11 how hydrogen bonding changes with increasing temperature. Although a hydrogen bonding analysis was presented previously by Bergenstråhle *et al.*,[33] their analysis is incomplete, focusing on only a subset of all intrachain and interchain hydrogen bonds, and lacking comparison with experiment. In Fig. 11, we see that increasing temperature from 300 K to 550 K decreases the total number of hydrogen bonds by only 20%. This is surprising, given the substantial change in the IR spectrum over this temperature range. To understand this persistence of hydrogen bonding, we have tracked the numbers of intrachain and interchain hydrogen bonds, shown also in Fig. 11. Intrachain hydrogen bonds are responsible for chain conformation stability, whereas interchain hydrogen bonds are responsible for sheet stability.[27] We find in Fig. 11 with the increase in temperature there is substantial rupture of intrachain hydrogen bonds by 450 K, approximately balanced by formation of new interchain hydrogen bonds. Thus, many of the OH groups involved in intrachain hydrogen bonding at low temperature form interchain hydrogen bonds at higher temperatures, producing a high temperature structure with more stable sheets. The presence of such a high temperature crystalline structure is supported by XRD experiments,[29,30] which observe a sudden change in the cell parameters (see Fig. 5). This additional sheet stability attributed to the

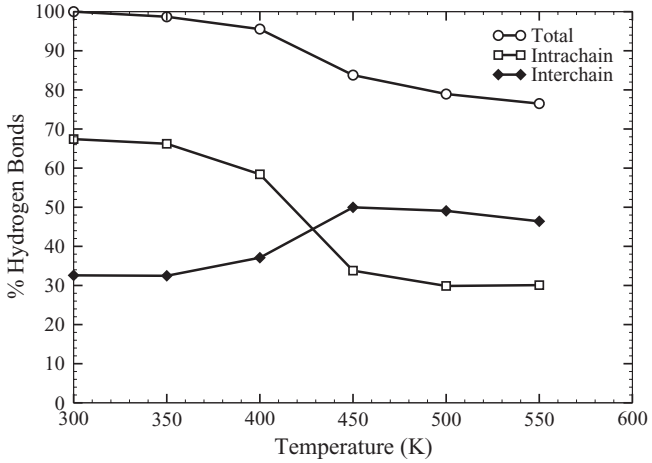

FIG. 11. Gross changes in hydrogen bonding with temperature, plotted as the percentage of total hydrogen bonds present at 300 K.

formation of a three-dimensional hydrogen bonding pattern may explain why cellulose does not melt below 550 K.

We show in Fig. 12 how heating changes the numbers of specific hydrogen bonds. We see from Fig. 12 that there are dramatic changes in the numbers of all the hydrogen bonds around 400–450 K except for O3H3···O5 intrachain bonds, which show only a gradual decrease with temperature. We observe essentially complete breaking of O2H2···O6 intrachain bonds by 450 K, leading to the formation of O2H2···O6 and O2H2···O3 interchain hydrogen bonds. Watanabe *et al.*[32] have shown through two-dimensional correlation IR spectroscopy that O2H2···O6 intrachain hydrogen bonds completely break around 490 K, matching reasonably well with our modeling results. Our underestimation of this transition temperature suggests our simulation slightly underestimates the strengths of cellulose hydrogen bonds, consistent with our slight underestimation of the total dipole moment and the static dielectric constant.

Watanabe *et al.*[32] have reported that O3H3···O5 intrachain hydrogen bonds also rupture suddenly around 490 K. In contrast, we find only a slight (∼20%) decrease

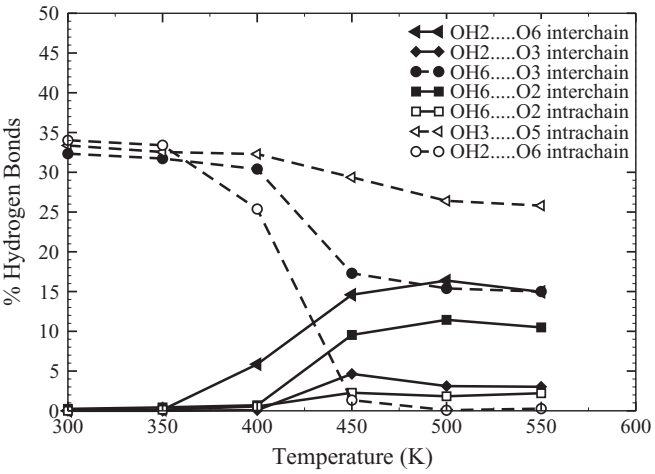

FIG. 12. Detailed changes in hydrogen bonding with temperature, plotted as the percentage of total hydrogen bonds present at 300 K.

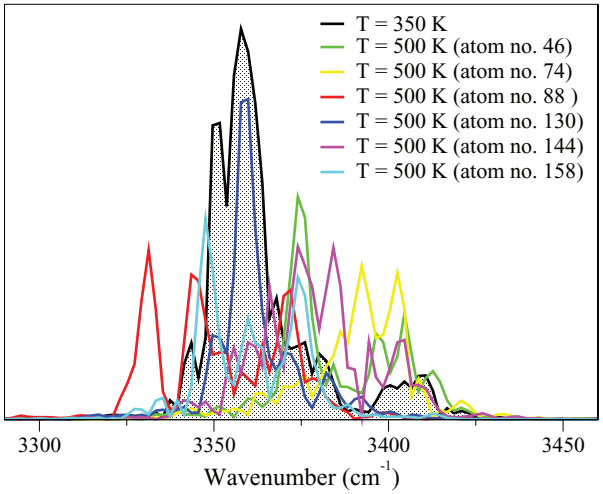

FIG. 13. Average power spectrum over all O3H3 atoms for low temperature (350 K), and individual power spectra of six O3H3 atoms at high temperature (500 K).

in the number of O3H3···O5 hydrogen bonds in our simulations from 300–550 K. An important thing to note here is that the conclusion of Watanabe *et al.*[32] regarding the rupture of O3H3···O5 bonds is based on assignments made by Maréchal and Chanzy.[35] In particular, Watanabe *et al.*[32] drew this conclusion because of the disappearance upon heating of the main OH-stretching IR peak at 3341 cm^{-1}, which Maréchal and Chanzy[35] assigned solely to the O3H3 stretch. Our results (Fig. 8) show that this main peak receives contributions from both O3H3 and O2H2 vibrations, indicating that a revision to the assignments of Maréchal and Chanzy is warranted.

Focusing now just on the O3H3 vibrations upon heating, we find inhomogeneous broadening to contribute to the disappearance of the sharp feature in the high-temperature IR spectrum of cellulose. To illustrate this point, we show in Fig. 13 the average power spectrum over all H3 atoms at 350 ± 5.9 K, as well as individual power spectra for six selected H3 as representations of all H3 atoms at 500 ± 8.4 K. The power spectrum at 350 K shows the same distinct feature present in the IR spectrum at that temperature. The power spectra at 500 K tell a different story. Although each of these spectra is relatively localized with widths around 20 cm^{-1}, an average over all these as occurs in the IR spectrum washes out the distinct features, producing an inhomogeneously broadened spectrum with a width around 80 cm^{-1}. Thus, we suggest that the loss upon heating of the main OH-stretching IR peak is not due to breaking O3H3···O5 hydrogen bonds, but rather from thermal fluctuations that produce several distinct O3H3 environments.

IV. CONCLUSIONS

We performed molecular dynamics simulations using a united-atom forcefield to investigate the physical effects of heating cellulose Iβ. The GROMOS 45a4 forcefield was tested by computing the following thermophysical properties of cellulose Iβ at room temperature: density, thermal expansion

coefficients, total dipole moment, and the static dielectric constant. These computed properties were found to be in sufficient agreement with experiments. Our simulations predict a relatively sudden change in density between 400 and 450 K, indicating a structural change to cellulose Iβ. A decrease in the unit cell parameter b and, hence, a negative thermal expansion coefficient was found from simulations at high temperatures, in qualitative agreement with experiments. This result arises from rotation of cellulose chains along their chain axis.

The IR spectrum of cellulose Iβ was computed at room temperature, showing only a qualitative match with experiment at lower frequencies because of the united-atom approximation. Agreement with experiment is much better at higher frequencies, in the OH stretching region. A novel synthesis of normal mode analysis and power spectrum methods was used to assign the three distinct IR features in the OH stretching region. Our assignment of the O6H6 motion to the highest frequency feature at 3410 cm^{-1} is in good agreement with previous interpretations. Our results show that the two lower frequency IR features involve mixtures of O2H2 and O3H3 vibrations; this stands in contrast to a previous assignment which assumes O2H2 vibrates at 3273 cm^{-1} and O3H3 at 3341 cm^{-1}.

The IR spectrum of cellulose Iβ was also computed at elevated temperatures. The computed IR spectrum suggests a structural transformation between 400 and 450 K. The low-temperature IR spectrum was found to have three distinct peaks, whereas the high-temperature IR spectrum lacked distinct features. In contrast to previous interpretations of the cause of this featureless spectrum, we find no disruption OH3$\cdots$O5 intrachain hydrogen bonds. Instead, we found that the featureless IR spectrum above 450 K is due to inhomogeneous broadening of O3H3 stretching bands. The structural transition of cellulose Iβ was found to arise from the disruption of O2H2$\cdots$O6 intrachain hydrogen bonds, which convert to interchain hydrogen bonds. The low-temperature structure (300–425 K) of cellulose Iβ was found to have dominance of intrachain hydrogen bonds, whereas the high temperature structure (425–550 K) has dominance of interchain hydrogen bonds. A three-dimensional hydrogen bonding network is observed at high temperature due to formation of new interchain and intersheet hydrogen bonds, which may explain the stability of cellulose structure at such high temperatures. In future work, we will investigate the chemical transformation of high-temperature cellulose Iβ to levoglucosan.

ACKNOWLEDGMENTS

We thank Professor Paul J. Dauenhauer, Dr. JoungMo Cho, and the entire EFRI team at UMass Amherst for stimulating discussions on cellulose pyrolysis. This material is based upon work supported by the National Science Foundation under the Emerging Frontiers in Research and Innovation program (EFRI) 0937895.

[1] T. Bridgwater, Biomass Bioenergy **31**, vii (2007).
[2] A. Demirbas and G. Arin, Energy Sources, Part A: Recovery, Util., and Environ. Eff. **24**, 471 (2002).
[3] M. Demirbas and M. Balat, J. Sci. Ind. Res. **66**, 797 (2007).
[4] T. Carlson, T. Vispute, and G. Huber, ChemSusChem **1**, 397 (2008).
[5] G. W. Huber, S. Iborra, and A. Corma, Chem. Rev. **106**, 4044 (2006).
[6] A. Bridgwater, D. Meier, and D. Radlein, Org. Geochem. **30**, 1479 (1999).
[7] B. Babu, Biofuels, Bioprod. Biorefin. **2**, 393 (2008).
[8] D. Mohan, C. U. Pittman, and P. H. Steele, Energy Fuels **20**, 848 (2006).
[9] S. Pèrez and K. Mazeau, in *Polysaccharides: Structural Diversity and Functional Versatility*, 2nd ed., edited by S. Dumitriu (Marcel Dekker, New York, 2005), Chap. 2, pp. 41–68.
[10] J. Diebold, Biomass Bioenergy **7**, 75 (1994).
[11] F. Shafizadeh and a. G. W. Bradbury, J. Appl. Polym. Sci. **23**, 1431 (1979).
[12] A. G. W. Bradbury, Y. Sakai, and F. Shafizadeh, J. Appl. Polym. Sci. **23**, 3271 (1979).
[13] J. A. Conesa, J. A. Caballero, A. Marcilla, and R. Font, Thermochim. Acta **254**, 175 (1995).
[14] J. Piskorz, D. Radlein, and D. Scott, J. Anal. Appl. Pyrolysis **9**, 121 (1986).
[15] Y.-C. Lin, J. Cho, G. a. Tompsett, P. R. Westmoreland, and G. W. Huber, J. Phys. Chem. C **113**, 20097 (2009).
[16] J. Cho, J. M. Davis, and G. W. Huber, ChemSusChem **3**, 1162 (2010).
[17] R. K. Agrawal, Can. J. Chem. Eng. **66**, 413 (1988).
[18] R. K. Agrawal, Can. J. Chem. Eng. **66**, 403 (1988).
[19] S. Alves and J. Figueiredo, J. Anal. Appl. Pyrolysis **17**, 37 (1989).
[20] M. J. Antal, G. Várhegyi, and E. Jakab, Ind. Eng. Chem. Res. **37**, 1267 (1998).
[21] V. Mamleev, S. Bourbigot, and J. Yvon, J. Anal. Appl. Pyrolysis **80**, 141 (2007).
[22] O. Boutin, M. Ferrer, and J. LéDé, J. Anal. Appl. Pyrolysis **47**, 13 (1998).
[23] Q. Liu, S. Wang, K. Wang, X. Guo, Z. Luo, and K. Cen, Acta Phys. Chim. Sin. **24**, 1957 (2008).
[24] J. Lédé, F. Blanchard, and O. Boutin, Fuel **81**, 1269 (2002).
[25] C. Somerville, Annu. Rev. Cell Dev. Biol. **22**, 53 (2006).
[26] R. H. Atalla and D. L. Vanderhart, Science **223**, 283 (1984).
[27] M. Jarvis, Nature (London) **426**, 611 (2003).
[28] Y. Nishiyama, G. P. Johnson, A. D. French, V. T. Forsyth, and P. Langan, Biomacromolecules **9**, 3133 (2008).
[29] M. Wada, J. Polym. Sci., Part B: Polym. Phys. **40**, 1095 (2002).
[30] M. Wada, R. Hori, U.-J. Kim, and S. Sasaki, Polym. Degrad. Stab. **95**, 1330 (2010).
[31] A. Watanabe, S. Morita, and Y. Ozaki, Appl. Spectrosc. **60**, 611 (2006).
[32] A. Watanabe, S. Morita, and Y. Ozaki, Biomacromolecules **7**, 3164 (2006).
[33] M. Bergenstråhle, L. A. Berglund, and K. Mazeau, J. Phys. Chem. B **111**, 9138 (2007).
[34] J. F. Matthews, M. Bergenstråhle, G. T. Beckham, M. E. Himmel, M. R. Nimlos, J. W. Brady, and M. F. Crowley, J. Phys. Chem. B **115**, 2155 (2011).
[35] Y. Maréchal and H. Chanzy, J. Mol. Struct. **523**, 183 (2000).
[36] R. G. Gordon, Adv. Magn. Reson. **3**, 1 (1968).
[37] R. Ramírez, T. López-Ciudad, P. Kumar, and D. Marx, J. Chem. Phys. **121**, 3973 (2004).
[38] M. Van Houteghem, T. Verstraelen, D. Van Neck, C. Kirschhock, J. A. Martens, M. Waroquier, and V. Van Speybroeck, J. Chem. Theory Comput. **7**, 1045 (2011).
[39] M. Martinez, M.-P. Gaigeot, D. Borgis, and R. Vuilleumier, J. Chem. Phys. **125**, 144106 (2006).
[40] M. Schmitz and P. Tavan, J. Chem. Phys. **121**, 12233 (2004).
[41] K. Smirnov and D. Bougeard, Catal. Today **70**, 243 (2001).
[42] J. J. Cael, K. H. Gardner, J. L. Koenig, and J. Blackwell, J. Chem. Phys. **62**, 1145 (1975).
[43] W. R. P. Scott, P. H. Hünenberger, I. G. Tironi, A. E. Mark, S. R. Billeter, J. Fennen, A. E. Torda, T. Huber, P. Krüger, and W. F. van Gunsteren, J. Phys. Chem. A **103**, 3596 (1999).
[44] Y. Nishiyama, P. Langan, and H. Chanzy, J. Am. Chem. Soc. **124**, 9074 (2002).
[45] See supplementary material at http://dx.doi.org/10.1063/1.3646306 for electrical flux-flux correlation function, effect of system size on IR spectrum of cellulose Iβ at 300 K, and high-frequency vibrational modes of glucose.
[46] M. J. Frisch, G. W. Trucks, H. B. Schlegel *et al.*, GAUSSIAN03, Revision D.02, Gaussian, Inc., Wallingford, CT, 2004.
[47] K. Mazeau, Cellulose **12**, 339 (2005).
[48] D. van der Spoel, E. Lindahl, B. Hess, A. R. van Buuren, E. Apol, P. J. Meulenhoff, D. P. J. Tieleman, A. L. T. M. Sijbers, K. A. Feenstra, R. van Drunen, and H. J. C. Berendsen, gromacs user manual version 4.0, University of Groningen, Netherlands, 2005; see http://www.gromacs.org.

[49]R. D. Lins and P. H. Hunenberger, J. Comput. Chem. **26**, 1400 (2005).
[50]C. a. Stortz, G. P. Johnson, A. D. French, and G. I. Csonka, Carbohydr. Res. **344**, 2217 (2009).
[51] W. F. van Gunsteren, S. Billeter, A. Eising, P. Hünenberger, P. Krüger, A. Mark, and W. Scott, *Biomolecular Simulation: The* GROMOS *96 Manual and User Guide* (vdf Hochschulverlag AG an der ETH Zürich and BIOMOS b.v., Zürich, Groningen, 1996).
[52] D. Frenkel and B. Smit, *Molecular Simulation: From Algorithms to Applications* (Academic, California, 2002).
[53] M. P. Allen and D. J. Tildesely, *Computer Simulation of Liquids* (Oxford University Press, New York, 1987).
[54]T. Darden, D. York, and L. Pedersen, J. Chem. Phys. **98**, 10089 (1993).
[55]S. Nosé, Mol. Phys. **52**, 255 (1984).
[56]W. Hoover, Phys. Rev. A **31**, 1695 (1985).
[57]P. H. Hünenberger, Adv. Polym. Sci. **173**, 105 (2005).
[58]H. J. C. Berendsen, J. P. M. Postma, W. F. van Gunsteren, A. DiNola, and J. R. Haak, J. Chem. Phys. **81**, 3684 (1984).
[59] D. A. McQuarrie, in *Statistical Mechanics*, 2nd ed. (Harper Collins, New York, 1976).
[60] D. Chandler, *Introduction To Modern Statistical Mechanics* (Oxford University Press, New York, 1987).
[61]D. W. Noid, M. L. Koszykowski, and R. A. Marcus, J. Chem. Phys. **67**, 404 (1977).
[62]P. Bornhauser and D. Bougeard, J. Phys. Chem. B **105**, 36 (2001).
[63] E. Kreszig, *Advanced Engineering Mathematics*, 8th ed. (Wiley, Delhi, 1999).
[64]B. Boulard, J. Kieffer, C. C. Phifer, and C. A. Angell, J. Non-Cryst. Solids **140**, 350 (1992).
[65]M. Praprotnik and D. Janezic, J. Chem. Phys. **122**, 174103 (2005).
[66]F. J. Harris, Proc. IEEE **66**, 51 (1978).
[67]P. H. Berens and K. R. Wilson, J. Chem. Phys. **74**, 4872 (1981).
[68]E. Jaramillo, C. P. Grey, and S. M. Auerbach, J. Phys. Chem. B **105**, 12319 (2001).
[69] S. W. Smith, *Digital Signal Processing: A Practical Guide for Engineers and Scientists* (Newnes, Boston, 2003), pp. 277–279.
[70]S. A. Egorov and J. L. Skinner, Chem. Phys. Lett. **293**, 469 (1998).
[71]S. C. Turaga and S. M. Auerbach, J. Chem. Phys. **118**, 6512 (2003).
[72] S. K. Gupta, *Numerical Methods for Engineers* (Wiley Eastern, New Delhi, 1995).
[73] W. H. Press, S. A. Teukolsky, W. T. Vetterling, and B. P. Flannery, in *Numerical Recipes in C: The Art of Scientific Computing*, 2nd ed. (Cambridge University Press, Harayana, 1992).
[74] E. B. Wilson, Jr., J. C. Decius, and P. C. Cross, *Molecular Vibrations: The Theory of Infrared and Raman Vibrational Spectra* (McGraw-Hill, New York, 1955).
[75]J. Sugiyama, R. Vuong, and H. Chanzy, Macromolecules **24**, 4168 (1991).
[76]M. Takahashi and H. Takenaka, Polym. J. **14**, 675 (1982).
[77]A. P. Heiner, J. Sugiyama, and O. Teleman, Carbohydr. Res. **273**, 207 (1995).
[78]J. Bird, N. Brough, S. Dixon, and S. N. Batchelor, J. Phys. Chem. B **110**, 19557 (2006).
[79]B. Jennings and J. Schweitzer, Eur. Polym. J. **10**, 459 (1974).
[80]S. K. K. Jatkar and D. S. Sastry, J. Univ. Poona Sci. Technol. **4**, 55 (1953).
[81]K. Araki and Y. Imamura, Die Makromolekulare Chemie **183**, 1343 (1982).
[82]E. J. Cocinero, D. P. Gamblin, B. G. Davis, and J. P. Simons, J. Am. Chem. Soc. **131**, 11117 (2009).
[83]S. El-Henawtf, S. Saad, and I. El-Anwar, J. Mater. Sci. Technol. **15**, 164 (1999).
[84]M. Tsuboi, J. Polym. Sci. **25**, 159 (1957).
[85]J. Blackwell, P. D. Vasko, and J. L. Koenig, J. Appl. Phys. **41**, 4375 (1970).
[86]J. Blackwell, P. D. Vasko, and J. L. Koenig, Bull. Am. Phys. Soc. **15**, 305 (1970).
[87]C. Y. Liang and R. H. Marchessault, J. Polym. Sci. **37**, 385 (1959).
[88]C. Y. Liang and R. H. Marchessault, J. Polym. Sci. **39**, 269 (1959).
[89] G. C. Pimentel and A. L. McClellan, *The Hydrogen Bond* (Freeman, San Francisco, 1960).
[90]F. Horii, A. Hirai, and R. Kitamaru, Polym. Bull. **10**, 357 (1983).